Development of a droplet microfluidics device based on integrated soft magnets and fluidic capacitor for passive extraction and redispersion of functionalized magnetic particles

Marco Serra, Emilie Gontran, Ismail Hajjj, Laurent Malaquin, Jean-Louis Viovy, Stephanie Descroix, Davide Ferraro

Development of a droplet microfluidics device based on integrated soft magnets and fluidic capacitor for passive extraction and redispersion of functionalized magnetic particles

Marco Serra, Emilie Gontran, Ismail Hajji, Laurent Malaquin, Jean-Louis Viovy, Stephanie Descroix, Davide Ferraro**

Dr. M. Serra, E. Gotran, Dr. I. Hajji, Dr. J.-L. Viovy, Dr. S. Descroix
Laboratoire Physico Chimie Curie, Institut Curie, CNRS UMR168, 75005 Paris, France
Institut Pierre-Gilles de Gennes, 75005 Paris, France
E-mail: stephanie.descroix@curie.fr

Dr. L. Malaquin
Laboratoire Physico Chimie Curie, Institut Curie, CNRS UMR168, 75005 Paris, France
Institut Pierre-Gilles de Gennes, 75005 Paris, France
LAAS-CNRS, Université de Toulouse, CNRS, INSA, Toulouse, France

Dr. D. Ferraro
Laboratoire Physico Chimie Curie, Institut Curie, CNRS UMR168, 75005 Paris, France
Institut Pierre-Gilles de Gennes, 75005 Paris, France
Department of Physics and Astronomy, University of Padua, 35131 Padua, Italy
E-mail: davide.ferraro@unipd.it

Keywords: droplet microfluidics, magnetic particles handling, fluidic capacitor, magnetic PDMS, droplet fingering

Based on a recent droplet microfluidic approach for target molecules extraction, purification and redispersion, we propose here an improved fluidic control to make this device more user friendly and reliable. This approach is based on the coupling of functionalized magnetic particles handling by integrated soft magnets and a passive droplet splitting control at a channel junction. To reach the high standards required for bioassays implementation, this device integrates a pressure-driven variable volume component, acting as a fluidic capacitor, which allows a passive and controlled self-triggered droplet fingering in a dead-end channel. The working principle is described and the modeling of the induced fingering phenomenon by an electric analogy is presented. Then, the achieved finger length is characterized as a function of geometrical and material properties of the fluidic capacitor.

The complete device configuration guarantees extraction and purification efficiencies higher than 97% and 95%, respectively, showing high throughput particles handling between droplets with a passive droplet splitting control. Finally, this technology is successfully applied to gene

expression study for cancer diagnosis by performing magnetic particles-based mRNA extraction followed by RT-qPCR analysis.

1. Introduction

In the last decade, droplet microfluidics developed as a mature technology[1], able to propose robust solutions for the automation and downscaling of complex workflows, as well as to foster innovations, notably for high-sensitivity detection[2,3] and single-cell analysis[4,5]. Among the different tools implemented in droplet microfluidics, strategies for functionalized magnetic particles handling recently gained a central role[6]. As a matter of fact, they allowed the implementation of several bioanalytical workflows relying on the enrichment or purification of target molecules prior to quantification or downstream processing. Among the different approaches proposed[6], continuous droplet microfluidic-based strategies have the advantage to deliver high throughput solutions. The first examples proposed rely on the splitting of a parent droplet in two daughter droplets at a T-junction, while an external magnet allows the enrichment of the magnetic particles in one of them[7,8]. This process is characterized by a complete recovery of the particles present in the parent droplet (high extraction efficiency[9]); however, the symmetric splitting strategy limits the purification efficiency ($\simeq$50%), which is defined as the depletion rate of the original matrix in the final purified solution[9]. Devoted strategies for inducing an asymmetric droplet splitting were also proposed, which can be divided in passive or active control methods. In the former, the droplet splitting is regulated by tuning the microchannel geometries, thus their hydraulic resistance ratio at the junction[10,11], but still obtaining a poor purification rate. To further improve this aspect, specific design features exploiting capillary effects were also proposed[12]. However, this strategy is dependent on the droplet speed, notably being progressively ineffective with increasing flow-rates; therefore, devoted modifications on the microchannels design must be adopted to preserve the performance at different flow-rates.

Differently, active strategies rely on a dynamic flow regulation through external pumps to induce an asymmetric droplet splitting at a symmetric T-junction geometry[13,14]. Therefore, the asymmetric droplet splitting can be adjusted according to its speed, without the need for geometrical device modifications. Nevertheless, active approaches require an external pumping device, thus increasing the cost and the complexity of the overall setup. Importantly, using both active and passive approaches, the devices presented so far allow uniquely the enrichment of magnetic particles within a daughter droplet, thus preventing the redispersion of particles-binding purified molecules into a new solution. Consequently, the implementation of multi-step workflows would require devoted merging modules[15,16]. We recently proposed an active control method consisting in a device allowing the tuning of the droplet deformation at a T-junction by an external pressure-based system, coupled with integrated soft magnets for particles handling[9]. Together with high purification rate, this approach guarantees particles extraction from a droplet and redispersion in a different one, being suitable for multi-step protocols. Additionally, differently than previously reported methods for extraction/redispersion protocols[6,17], it allows higher integration, scalability and analysis throughput. However, as the other active approaches, it requires a fine pressure control at the junction to carefully tune the droplet deformation according to its speed, to avoid an undesired spontaneous droplet break-up as well as to guarantee optimal purification and extraction rates.

Here, to overcome the limitations of both passive and active approaches in the droplet splitting, we present an improvement of our recent work[9], which integrates the soft magnets concept with a pressure-driven variable volume component in a dead-end channel, describing a passive system that ensures efficient extraction and redispersion processes in a wide range of droplet speeds. Notably, this original module behaves like a fluidic capacitor, which is triggered by the dynamic pressure drop caused by a confined droplet flowing across a channel junction. A few examples of integrated microfluidic capacitors were already proposed to dump the oscillations caused by an external pump[18] or to implement flow control strategies[19–21]. Despite these

represent elegant approaches with respect to the use of external valve systems, they are not optimized for droplet handling.

In order to evaluate the effect of the fluidic capacitor on the magnetic particles handling performances, at first, we considered a simple T-junction channel configuration presenting a dead-end pocket (capture region or trap) in-between the soft magnets (see **Figure 1a**). This configuration allows the deflection of magnetic particles, initially confined in a parent droplet, towards the trap. Furthermore, it causes the droplet splitting at the junction and leads to the generation of a daughter droplet, enriched with particles and characterized by an extremely low carryover of supernatant, which is retained in the trap. This sub-droplet can be then redispersed in a new droplet, assuring the capability to release the target molecules in a different solution. Then, we developed a novel microfluidic capacitor and connected it to the transversal dead-end channel (**Figure 1b**). This element, triggered by the dynamic presence of the droplet in the channel, allows a passive self-control of the droplet penetration (or fingering) in-between the magnetic elements. This preserves the device functionalities above described, while guaranteeing improved extraction capabilities in a wide range of flow-rates without the need for any external pumping system.

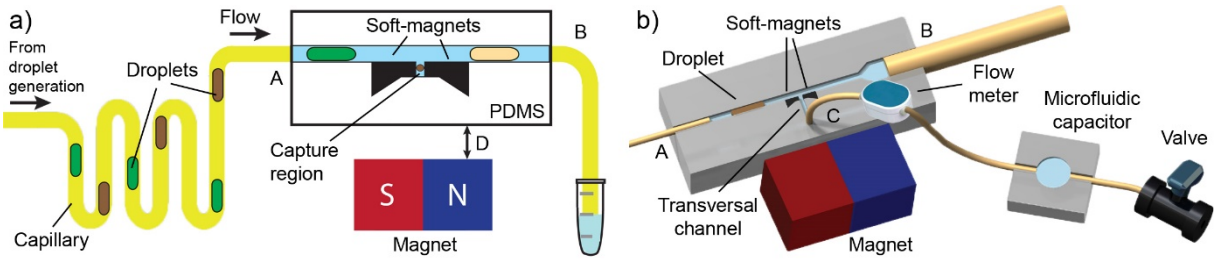

Figure 1: *Overview of the experimental setup. a) Droplets flow towards the microfluidic device integrating the pair of soft magnetic components adjacently to the main channel. The portion of the channel between the soft magnetic components defines the capture region (or trap), where the extracted magnetic cluster will be accommodated. The integrated microstructures are activated by an external permanent magnet, placed at a distance D, which can be varied to control the status (ON/OFF) of the microstructures. b) The capture region is connected through*

a transversal channel to the fluidic capacitor. The outlet of this additional component is connected to a valve, kept closed during the entire experimental workflow in order to define a dead-end channel. Furthermore, a flow-meter is included to monitor the flow-rate in this fluidic section during the experiment.

In the following, at first, the microfabrication workflows and the working principle of the device in absence and presence of the fluidic capacitor will be presented. Then, the numerical and experimental optimization of the soft magnetic microstructures as a function of different PDMS doping concentrations are evaluated. To identify the optimal device features, different materials and geometry of the fluidic capacitor will be discussed, followed by a characterization of the device performances. Finally, to demonstrate the potential of this system, it has been exploited to implement a multi-step mRNA purification workflow, followed by reverse transcription (RT) and quantitative Polymerase Chain Reaction (qPCR), showing successful expression level determination of relevant genes for breast cancer diagnosis[22].

2. Results and Discussion

2.1. Microfluidic devices fabrication

A devoted microfabrication protocol, based on replica molding technique with polydimethylsiloxane (PDMS), is developed to integrate two soft magnetic microstructures. As shown in **Figure 2**, the device is composed of two PDMS parts: a top one including the microstructures and a bottom one presenting a longitudinal microchannel (width: 300 µm, height: 200 µm) with a dedicated pocket for their accommodation. For the top part, a CycloOlefin copolymer master, which presents two pockets on its surface defining the magnetic structures design, is produced by hot-embossing. Then, a mixture of PDMS and ferromagnetic iron powder is poured on the master to fill the pockets (**Figure 2a,i**). Three different Fe/PDMS ratios have been investigated (44.0, 60% and 70% w/w, corresponding to relative magnetic permeability μ_r= 1.301, 1.612, 1.883, respectively[23],[24]), in order to determine the iron doping

concentration effect on the extraction efficiency. We experimentally verified that the latter concentration represents the highest ratio guaranteeing reproducible PDMS curing. After vacuum degassing, the excess of magnetic PDMS is removed using a silicon blade[25] (**Figure 2a,ii**) and a conventional PDMS pre-polymer mixture is poured on the master (**Figure 2a,iii**). The whole system is then cured in an oven at 70°C for 48h. Notably, the long curing time is required by the presence of the iron powder. After that, the resulting flat PDMS layer with vertical magnetic structures is peeled-off from the master (**Figure 2a,iv**). Differently, the bottom part of the device is produced by conventional replica molding (**Figure 2a,v**). Finally, the two parts are aligned and bonded by oxygen plasma treatment.

Then, for the experiments including the microfluidic capacitor, the bottom part of the device is modified by introducing an additional transversal channel having a rectangular cross-section (width: 100 µm, height: 200 µm). This leads to a second outlet, which is connected to the fluidic capacitor during the experiment. **Figure 2b and 2c** report the images of the final device including the soft magnetic structures (see also SI Figure S4), with and without the transversal channel respectively.

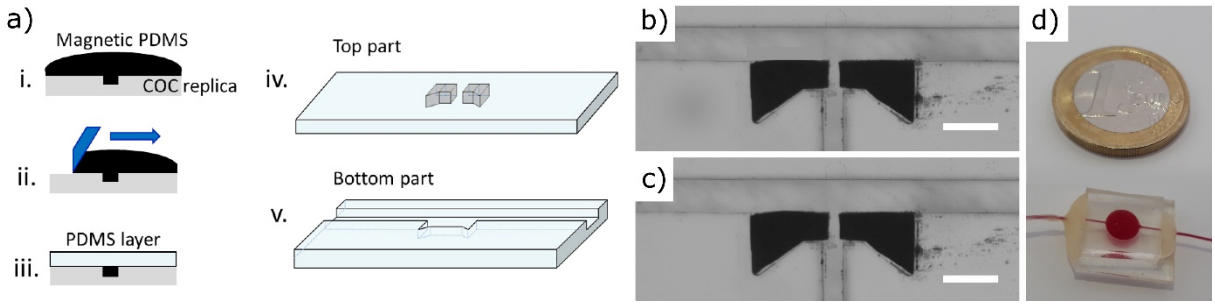

Figure 2: *a) Workflow of the integrated magnetic components fabrication (i-iii). A flat PDMS layer of few millimeters with two extruded micrometric magnetic structures is obtained (iv). These structures will be inserted in a dedicated pocket, designed in the bottom part of the device, also including the main channel for droplet flow (v). Based on this workflow, two devices are fabricated, characterized by a side-channel pocket (b) and an additional transversal channel (c), respectively. Scale bar: 500 µm. d) Image of the fluidic capacitor fabricated by double replica molding with either PDMS or Ecoflex. A red dye is used to highlight the device geometry.*

The fluidic capacitor, shown in **Figure 2d**, consists of a separated microfluidic chip having a circular shape of different radius (R=1.00 mm, 2.80 mm and 3.84 mm) and fixed height (200 µm), with an inlet and an outlet. Since the fluidic capacitor is a deformable unit, in order to investigate the effect of the material stiffness on the resulting droplet deformation, two materials typically used in microfluidics and characterized by different elastic moduli are considered: Sylgard 184 PDMS and Ecoflex 00-50. The former is prepared by double replica molding using a 20:1 base/curing agent w/w formulation to achieve higher elasticity than conventional PDMS (elastic modulus=0.50 MPa)[26]; differently, the latter is prepared by replica molding following the manufacturer's protocol (elastic modulus=0.20 MPa)[27,28]. Finally, the unmolded structures are bonded on a flat surface of the same material by oxygen plasma.

2.2. Estimation of the generated magnetic force

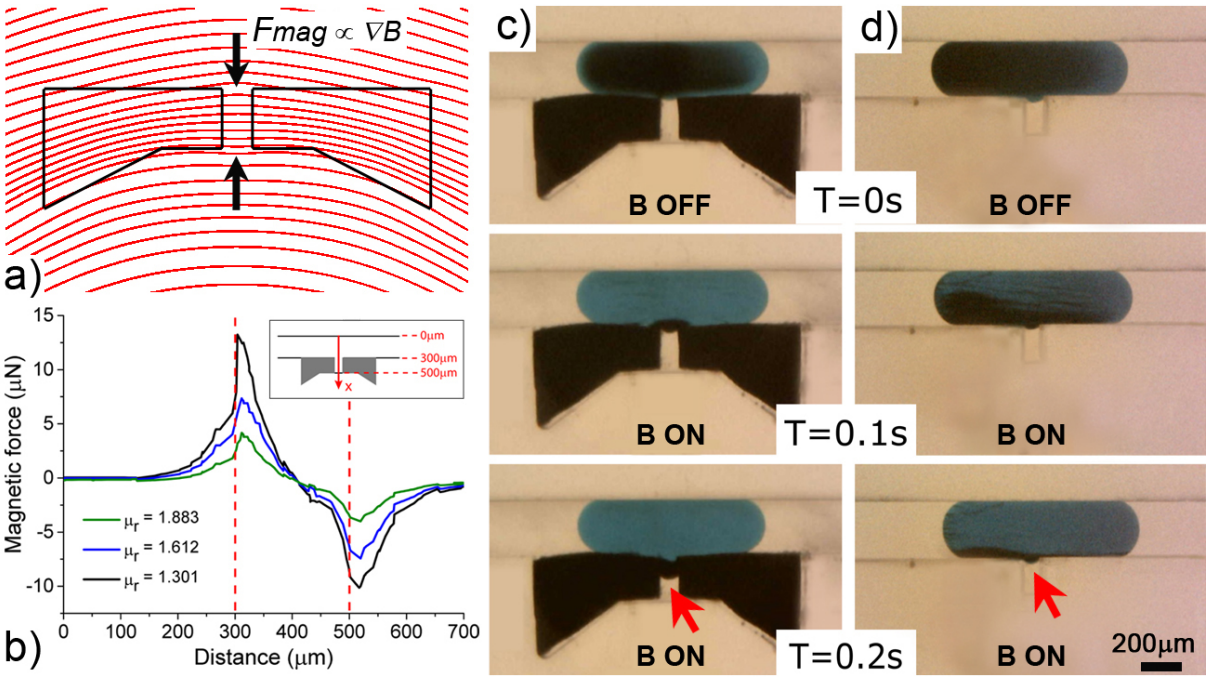

Figure 3: *a) Numerical simulation of the magnetic field streamlines distribution around the soft magnets. The streamlines density is higher in the trap region than outside, generating a* ∇B*, thus a* F_{mag}*, directed towards the centre of the capture region. (b) Magnetic force calculated on the symmetry axis of the integrated microstructures, as defined by the reference*

frame in the inset (c,d). Images sequence of the magnetophoretic displacement of particles confined in droplets triggered by the magnetic field (T=0s). Notably, only in presence of the integrated soft magnets, the particles exert a sufficiently pressure, able to deform the droplet meniscus in the trap region.

During the experiment, an external permanent magnet is placed near the device to magnetize the integrated soft magnets, as shown in **Figure 1a and 1b**. We present here an extension of a previous model[9] in which, using this configuration, the magnetic field streamlines result focalized in the side channel portion delimited by the microstructures (see **Figure 3a**). This leads to a locally higher magnetic flux density gradient (**∇B**) that causes a magnetic force ($\boldsymbol{F_{mag}}$) driving the magnetic particles in the capture region. This is also highlighted in **Figure 3b** where $\boldsymbol{F_{mag}}$, evaluated on the symmetry axis of the structures, results always directed towards the trap (according to the reference system described in **Figure 3b**, inset).

Together with the $\boldsymbol{F_{mag}}$ direction, its intensity is also relevant for the extraction process. Since the magnetic particles are confined in a droplet, a sufficient pressure, able to deform the droplet interface in the capture region, is required for their extraction. In **Figure 3b**, the resulting $\boldsymbol{F_{mag}}$ presents a maximum in the main channel and decreases in intensity approaching the trap, being zero in the centre of the pocket. Additionally, the influence of the PDMS doping concentration in the composite soft magnetic structures is investigated. As a matter of fact, the doping concentration affects the relative magnetic permeability of the composite, thus the induced magnetic flux density. In this study, three doping ratios (Fe/PDMS) are considered, i.e. 44%, 60% and 70% w/w and the resulting $\boldsymbol{F_{mag}}$ are reported in **Figure 3b**. As expected, an increase in iron concentration leads to the generation of higher magnetic forces. Interestingly, despite a small change in relative permeability (from μr=1.301 to μr=1.612), the resultant forces almost doubled, passing from 3.9 μN to 7.4 μN, and reaching a maximum of about 13.3 μN for μr=1.883. Considering the portion of the droplet interface in correspondence to the capture region (A=100 μm x 200 μm), the pressure exerted on it by the magnetic cluster (ΔP_M) can be

calculated as $\Delta P_M = F_{mag}/A$. Therefore, the highest F_{mag} generates a pressure $\Delta P_M \simeq 665$ Pa, which is higher than the Laplace pressure of the droplet meniscus (≃223.5 Pa), evaluated on the same area. This suggests that the pressure exerted by the magnetic particles allows the droplet interface deformation in the capture region, as experimentally demonstrated in **Figure 3c**, where a droplet is kept in a static condition (no applied flow in the channel) near the capture region and the magnetic field is successively activated (see also **Movie S1**). Notably, only in the presence of the soft-magnetic structures (**Figure 3c**) the generated magnetic force is able to drive the particles in the trap region, while the mere presence of the permanent magnet (**Figure 3d**) cannot lead to a significant droplet deformation, preventing any particles extraction in the trap.

2.3. Characterization of the extraction and redispersion processes

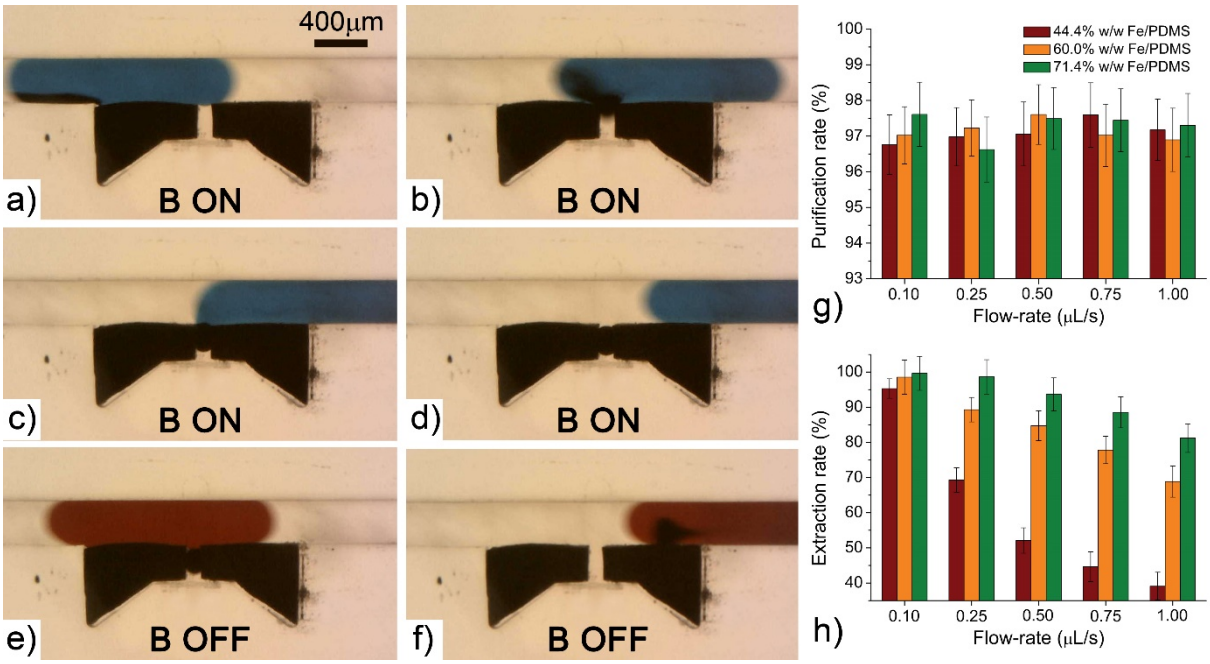

Figure 4: *(a-f) Sequence of images describing magnetic particles handling between different droplets. The integration of soft magnetic components allowed their extraction (a-d) from a parent droplet (in blue) and the following redispersion (e-f) in a droplet of different content (in red), by controlling the distance between the permanent magnet and the integrated microstructures. The device extraction (g) and purification (h) performances were evaluated*

as a function of the carrier oil flow-rate for different iron powder doping concentrations in PDMS.

In the first configuration (in absence of the microfluidic capacitor), characterized by a side dead-end channel as capture region, the integrated soft magnetic microstructures allow the exchange of magnetic particles between different droplets, mediated by extraction and redispersion processes, as shown by the images sequence in **Figure 4** and in Movie S2. Here, a first droplet containing the magnetic particles flows in the device channel and the presence of an external permanent magnet, combined with the droplet recirculation flows, leads to the formation of a cluster of particles in the bottom rear of the droplet (**Figure 4a**). While the droplet approaches the integrated magnetic structures, $\boldsymbol{F_{mag}}$ attracts the cluster towards the capture region (**Figure 4b**). Consequently, the cluster deforms the droplet interface and generates a tiny droplet finger, penetrating the capture region and containing the cluster (**Figure 4c**). This finger induces the droplet splitting and the consequent generation of a small sub-droplet containing the particle cluster (**Figure 4d**). When a second droplet reaches the capture region, spontaneous coalescence with the extracted sub-droplet occurs (**Figure 4e**) and, by switching OFF the external magnetic field, the particles are redispersed in it (**Figure 4f**).

The extraction and purification performances of the device are evaluated as a function of the carrier oil flow-rate and for different PDMS doping conditions. The purification efficiency results higher than 95%, independently from the flow-rate (between 0.10 μL/s and 1.00 μL/s) and the doping ratio (see **Figure 4g**). Importantly, as described in the following, this is due to the magnetically controlled droplet splitting at the junction, which allows to minimize the carryover of supernatant from the parent droplet, protecting the extracted cluster. Differently, as expected, the extraction rate increases with the doping concentration, thus with the magnetic force (**Figure 4h**). Notably, for the highest doping concentration, the extraction efficiency results higher than 95% up to 0.25 μL/s and decreases for increasing flow-rates, reaching an

efficiency of about 80% at 1 μL/s. This behavior is due to the interplay between the droplet drag force dynamics, pushing the cluster longitudinally in the channel, and the magnetic force that attracts the beads towards the trap, perpendicularly to the main flow. In fact, in order to reach the trap, the particles cluster must deform the droplet interface and, even if this event is energetically favorable (see **Figure 3c**), its dynamics is slowed down by the droplet interfacial force. Consequently, for the highest flow-rates, a part or the whole cluster can be dragged away from the capture region before being trapped and keep flowing in the parent droplet. To prevent the cluster bumping into the droplet interface during the extraction process as well as to improve the extraction efficiency at higher flow-rates, the microfluidic device was coupled to the fluidic capacitor. This original module acts as a passive and magnetic force-independent system that aims at generating a controlled droplet fingering [29] in the trap region, able to accommodate the cluster of particles while guaranteeing a high extraction efficiency.

2.4. Effect of the fluidic capacitor on the droplet deformation

Due to the hyperelastic properties of the fabrication material[30], the fluidic capacitor is a pressure-driven variable volume component allowing a tunable flow of oil ϕ in the transversal dead-end channel. This ϕ acts inflating the capacitor in response to a pressure gradient. Therefore, the pressure drop due to the presence of a confined droplet flowing in a microchannel, pushed by the external flow-rate Φ, can be exploited to self-trigger its fingering in the capture region. Furthermore, as the pressure is stopped, the deformable unit is expected to deflate, recovering the initial condition.

In order to investigate and characterize the droplet fingering phenomenon, we performed a purely hydrodynamic study in absence of the magnet. **Figure 5a** describes a typical profile of the flow rate ϕ in the transversal channel in presence of a capacitor. Initially, when no oil flow is applied in the main channel (Φ=0 μL/s), ϕ=0 μL/s as expected; as soon as a constant oil flow

is set ($\Phi \neq 0$ μL/s), ϕ increases, reaching a maximum (blue box in **Figure 5a**) and then exponentially decreases in time, leading again to a steady state. Notably, two different regimes can be identified: i) a rest condition for $\Phi = 0$ μL/s anticipates the initial peak in flow-rate (**Figure 5a**, blue box) and ii) an inflated state follows the same peak for a constant flow-rate $\Phi \neq 0$ μL/s. Furthermore, stopping the flow, the fluidic capacitor completely deflates reaching the initial resting state, as described by the negative profile in **Figure 5a** (green box), symmetric to the one obtained during the initial inflation. Interestingly, this behaviour corresponds to the charging/discharging curve of a conventional electric capacitor placed in parallel to an electric circuit controlled by a constant current (see Note S1 in SI for more details). Moreover, as for the equivalent electric circuit, we experimentally verified (see next paragraph) that the maximum volumetric expansion attained by the fluidic capacitor depends on its stiffness (due to the fabrication material) and geometrical properties, as well as on the applied Φ. More interestingly, a characteristic peak is also observed when a droplet, transported by a constant flow-rate Φ (0.25 μL/s), crosses the T-shaped junction (**Figure 5a**, red box). The confined droplet increases locally the hydraulic resistance in the main channel (R_h), causing an extra pressure in the transversal one and, consequently, a variation in ϕ. A more detailed effect of the droplet transition in the device is reported in **Figure 5b**, observed by synchronizing the flow and the image acquisition. In detail, as soon as the front meniscus of the droplet crosses the junction region, R_h increases and ϕ rises above the equilibrium baseline (**Figure 5b-1**). Consequently, the droplet experiences a fingering phenomenon (**Figure 5b-2**) until reaching a maximum finger length corresponding to a shoulder peak in the flow profile (**Figure 5b-3**). Then, the finger moves backwards into the main channel pulled by the rest of the droplet, as shown by the slight decrease in ϕ, until the back droplet meniscus rids a part of the transversal channel (**Figure 5b-4**). The latter, combined with the presence of the entire droplet confined in the main channel leads to a further increase in R_h after the junction (**Figure 5b-5**), causing an

important increase of ϕ. As soon as the droplet is deconfined, ϕ decreases (**Figure 5b-6**) and the fluidic capacitor subsequently deflates (negative portion of the curve), restoring its equilibrium position according to the applied constant Φ, until the next droplet is processed. According with this result, the increase of the channel cross-section after the junction is fundamental to guarantee a uniform deformation for all the droplets in the train, making the system independent from their number (see Note S2 in SI). This characteristic profile in presence of the fluidic capacitor has been modelled by an electric circuit analogy of the microfluidic network[31], which considers variable resistors placed in parallel to a capacitor (see Note S1 in SI). Notably, the main features of the simulated peak profile (see inset of **Figure 5b**) match to the microfluidic ones. Additionally, for a more quantitative evaluation, the measured flow-rate ϕ and the simulated current (I) were normalized by the respective maximum values (ϕ_{max} and I_{max}). The comparison between the normalized values shows that the simulated electric circuit is in quantitative agreement with the experimental data, confirming that the droplet crossing the junction leads to a variation of R_h, which triggers the capacitor response.

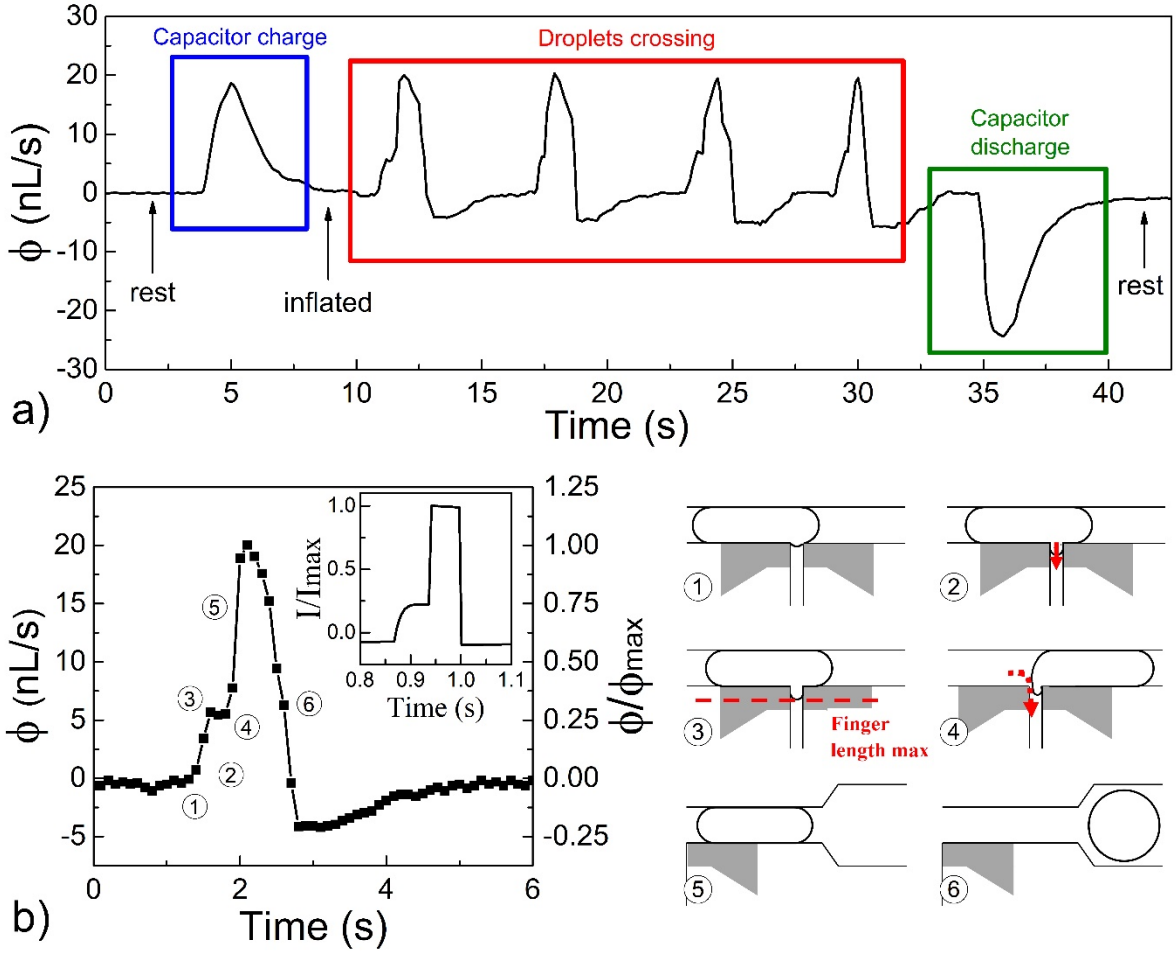

Figure 5: *a) Measured flow profile in the transversal dead-end channel containing a fluidic capacitor (Ecoflex, R=1 mm) during the flow of four droplets (100 nL) in the main channel (Φ = 0.25 µL/s). A flow inwards the capture region is indicated by a positive value. Three curve's features are stressed by coloured rectangles: i) initial capacitor charge due to the constant oil flow-rate pushing the droplet towards the device (blue); ii) crossing of four droplets (red); iii) capacitor discharge as the carrier flow is switched off (green). b) Flow profile during the crossing of a droplet. The profile features were associated to the corresponding position of the droplet in the device, as indicated by the sketches in the right part of the panel. This experimental profile was modeled by an electric analogy as reported in the inset.*

2.5. Fluidic capacitor's material and geometry characterization

Following the optimization of the channel geometry (See Note S2 in SI), the effect of the fluidic capacitor properties (stiffness and capacitor radius (R)) on the droplet fingering are investigated as a function of Φ. Importantly, **Figure 6** shows that, independently from the capacitor used, its presence leads to a longer finger length with respect to the case in which no variable-volume unit is present in the transversal channel; the latter case results indeed in a deformation of about 60 μm (empty black squares). Furthermore, different trends are observed according to the material used for the capacitor fabrication. Considering the PDMS capacitors (in red, elastic modulus=0.50 MPa), a constant finger length (about 120 μm) is measured for all R and Φ investigated, suggesting that the maximum volumetric expansion of the capacitor is reached. Differently, Ecoflex (in blue, elastic modulus=0.20 MPa) shows larger finger lengths than PDMS and an evident dependency on Φ. In detail, for a fixed R, the droplet finger lengths increase with Φ up to 0.25 μL/s, reaching a final plateau of about 160 μm and 185 μm for R=1.0 mm and R=2.8 mm, respectively. As in the PDMS case, this indicates that the capacitor reaches its maximum volumetric expansion in the range of considered flow-rates. On the other hand, the Ecoflex capacitor having R=3.84 mm (blue triangles) causes a droplet break-up for Φ>0.50 μl/s (no point reported in the graph).

These results clearly demonstrate that the introduction of the variable volume component in the transversal dead-end channel leads to a significant improvement of the fingering phenomenon which, additionally, depends on its material properties and size. Notably, the Ecoflex fluidic capacitor, characterized by a lower elastic modulus than PDMS, and thus by a lower stiffness and higher deformability, allows to induce a more important droplet deformation. However, the finger length must be finally tuned in order to avoid a spontaneous droplet break-up, which would negatively affect the extraction/purification efficiency. According with the obtained results, an Ecoflex device having R=2.80 mm will be used in the following.

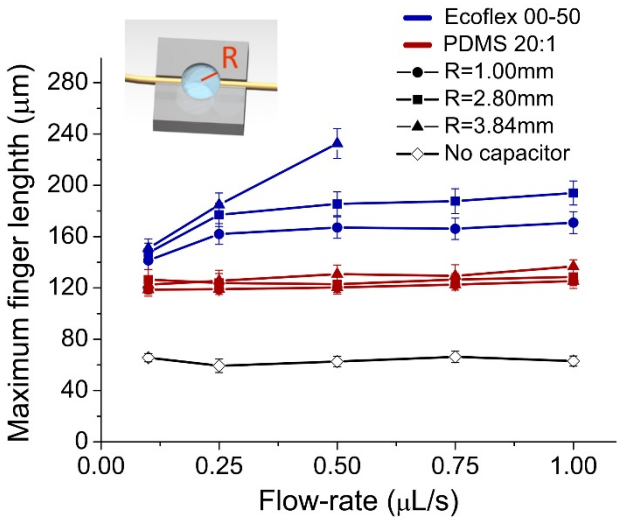

Figure 6: *a) Maximum droplet finger length as a function of the carrier oil flow-rate for different design conditions. Two fabrication materials, i.e. PDMS in a 20:1(w:w) base to curing agent formulation (represented as triangles) and Ecoflex 00-50 (represented by circles) were investigated. Different R were tested: R=1.00 mm (black points), 2.80 mm (red points) and 3.84 mm (blue points). A control experiment in absence of the fluidic capacitor in the transversal channel was also performed (empty black points).*

2.6. Evaluation of the extraction and purification efficiencies in presence of the fluidic capacitor

After the characterization of the fluidic capacitor, we investigated how its integration improves the extraction and redispersion efficiencies, also including a systematic comparison with the condition in absence of the fluidic capacitor. We first demonstrated that, combining the fluidic capacitor with activated magnetic microstructures (see **Figure 7**), the fingering process defines a droplet volume devoted to particles cluster accommodation in the capture region, prior to its magnetophoretic migration towards the trap (see red arrows in **Figure 7c-d**). This strategy allows the cluster to reach the trap without meeting any resistance from the droplet interface, leading to an important improvement in term of the extraction and the purification efficiencies as a function of Φ, as reported in **Figure 7i,j**. Notably, the coupling of the soft magnetic structures with the capacitor allows reaching a constant extraction rate higher than 97% for Φ up to 1.00 μL/s (**Figure 7j**, orange bars), as compared to about 80% in absence of the additional

component (green bars). The negligible amount (<2.5%) of beads that can be lost during the extraction process is related to the droplet pinch-off process prior to splitting, at the level of the channel junction. Importantly, the fluidic capacitor guarantees the magnetic particles to directly reach the trap region without bumping into the droplet interface, gaining a 2.5x factor in the time to reach the trap (see also Movie S3). Furthermore, differently from other continuous droplet microfluidics systems[12] in which a reduction in the extraction and purification efficiencies for increasing flow-rate is observed, here such reduction is not reported in the same range of investigated flow-rates thanks to the magnetically driven droplet splitting: the cluster keeps the droplet in a steady deformed state controlling its break-up (see **Figure 7f-h** and Movie S3) and, moreover, minimizing the carryover of supernatant in the enriched droplet. Finally, according with the investigated Φ, a maximum processing speed of about 17 mm/s can be achieved by our system for the whole extraction and redispersion process. Importantly, the presented system allows performances comparable with the previous active configuration[9] but exploiting a passive strategy therefore no tuning is required as a function of the processing velocity.

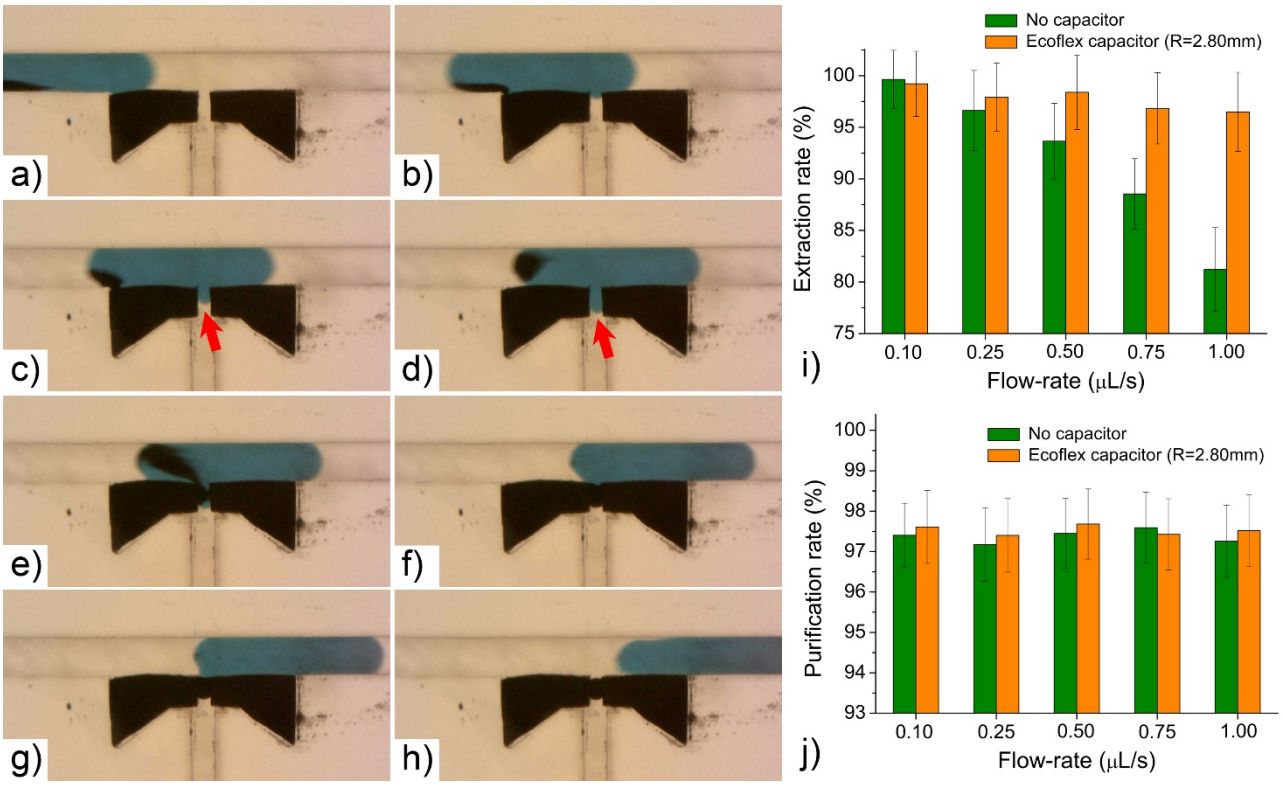

***Figure** 7: (a-h) Sequence of images showing the magnetic particles extraction with a system including the Ecoflex fluidic capacitor. The presence of the latter causes the droplet deformation in the capture region (c-d, red arrows) before particles magnetophoretic migration towards the same area (e-f). i-j) Extraction and purification efficiencies for 100nL droplets containing a particle load of 1µg as a function of the carrier oil flow-rate in the presence (orange bars) and absence (green bars) of the fluidic capacitor (Ecoflex, R=2.80 mm). This module guarantees extraction efficiencies higher than 97% for flow-rates up to 1.00 µL/s. The fluidic capacitor does not affect the purification efficiencies, which are always higher than 97%.*

2.7. mRNA purification from a total RNA sample

To illustrate the potential of this approach and to validate the reliability of both the magnetic particles handling and the self-regulating fluidic capacitor, we implemented a relevant bioassay for cancer diagnostic. In particular, we perform a double extraction and redispersion protocol devoted to mRNA purification from a total RNA sample extracted from a cancer cell line (SKBR3), followed by RT-qPCR in order to determine the expression level of two genes, Actin beta (ACTB) and Human Epidermal Growth factor 2 (HER2). The former is typically used as a reference gene[32], while the latter is an important biomarker for breast cancer[22].

As presented in **Figure 8a,i**, sequences of 3 droplets with deterministic composition are generated: 1) Oligo-dT surface functionalized magnetic beads; 2) Total RNA sample; 3) water. These droplet trains are consecutively flown across two microfluidic devices integrating the soft magnetic components. The first is exploited to extract the cluster of beads from the solution (**Figure 8a,ii-iii**) and to release them in the sample droplet (**Figure 8a,iv**). After 5 minutes of incubation time, required for mRNA target hybridization on Oligo-dT beads surfaces (**Figure 8a,v**), the latter are extracted by a second device and released in the coming water droplet (**Figure 8a,i**). These droplets are then collected in qPCR tubes for the final RT-qPCR analysis. Importantly, negative control experiments are performed substituting the sample with water in the second droplet of the train.

Calibration curves are performed using starting quantities of total RNA extracted from SKBR3 cell lines ranging from 2 ng/drop to 50 pg/drop. The results are reported in **Figure 8b**. Each point in the curve is the average of a triplicate experiment; the vertical error bars are given by the standard deviation while the horizontal error bars are evaluated taking into account the droplet volume variation. Notably, calibration curves present a linear and parallel tendency in the investigated range (R^2>0.99), proving that the mRNA capture achieved by the magnetic particles manipulation is reproducible over two orders of magnitude of total RNA concentrations. Additionally, taking into account that the droplets trains travel consequently in the same channel, no cross-contamination between them is observed, especially at the soft magnetic structures. The latter is also reinforced by the fact that the negative control does not show any positive results (see Figure S5 in SI).

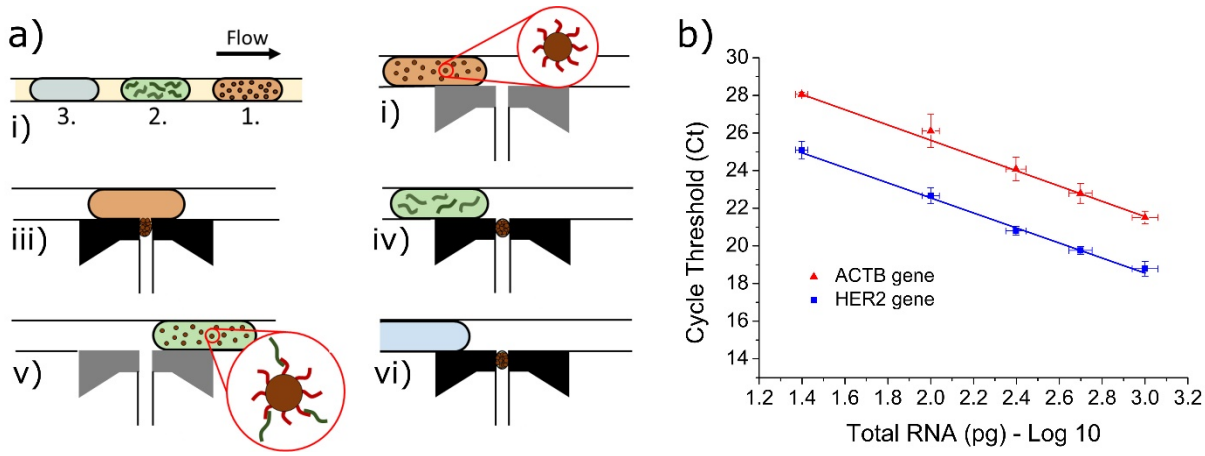

***Figure 8**: a) Scheme of the train composition and of the in-droplet mRNA purification workflow. Black and grey soft magnets indicate their ON and OFF state, respectively. b) Calibration curves performed with Total RNA extracted from SKBR3 cell line for HER2 (red) and ACTB (blue). The obtained Cycle Threshold (Ct) are plotted as a function of the Total RNA concentration.*

3. Conclusion

We presented an original strategy for magnetic particles handling in droplets based on integrated soft magnets and a passive control of the droplet splitting. Notably, the latter was achieved by exploiting the finger effect induced by a pressure-driven elastomeric component in

a dead-end channel, which acts as a fluidic capacitor. The numerical and experimental optimization of the PDMS doping concentration, as well as of the fluidic capacitor stiffness and size, allowed to achieve extraction and purification efficiencies higher than 97% and 95%, respectively, with a maximum processing velocity of 17 mm/s. Therefore, differently than previously reported passive approaches, this device shows high versatility allowing high extraction and purification efficiencies in a large range of flow rates (between 0.1 and 1μL/s), without requiring any further optimization. In addition, the possibility to exchange functionalized particles between different media with a minimum carryover of supernatant allowed the implementation of a multi-step mRNA purification protocol and the successful determination of gene expression level.

Finally, the presented device includes the main features required for the implementation of rapid and reliable extraction and enrichment multi-steps processes and can represent a key technology for the future down-scaling of further biochemical protocols.

4. Experimental Section

Microfabrication method details: The brass mold was obtained by a micromilling (Minitech Machinery) and used for the production of the CycloOlefin copolymer master by hot-embossing in the following conditions: 130°C at 5 bar for 40 min. The microfluidic device integrating the soft-magnetic structures was fabricated in PDMS (Sylgard 184, 10:1 base to curing agent ratio). Differently, as detailed above, this ratio has been adapted for the fluidic capacitor preparation. The iron power used for the fabrication of the soft-magnetic structures has a size distribution between 1 and 6μm (by GoodFellow). In order to bond the two PDMS parts (including the soft magnetic structures and the microchannel), they are initially activated by oxygen plasma, then aligned under a microscope using a film of ethanol spread in between the two surfaces and finally cured on a heating plate at 60°C for 30 min. Then, PTFE capillaries (OD/ID=0.6/0.3 mm and OD/ID=1.58/0.78 mm) are installed in the inlet and outlet

of the device, respectively. Finally, the internal channel surfaces are treated to improve the oil wetting, by (Tridecafluoro-1,1,2,2-tetrahydrooctyl)-trichlorosilane in FC-40 oil (5% v/v) for 20 min.

Experimental setup for droplet generation and handling: Aqueous phase droplets are generated by pipetting in FC-40 oil with 2% w/w surfactant (1H, 1H, 2H, 2H-perfluoro-1-decanol, by Fluorochem), using an arm-robot coupled with a syringe pump, as presented in Ferraro et al.[17]. The latter allows the generation of deterministic trains of droplets, sampled from a microtiter plate. Furthermore, the system allows to tune the flow-rate of the carrier fluid (Φ) independently from the droplet size, numbers and contents. Following the generation, the droplets are flown in the PFTE capillary towards the inlet A of the microfluidic device integrating the magnetic microstructures (see **Figure 1a**). Differently, the outlet B of the device (see **Figure 1a**) is kept at the atmospheric pressure in a reservoir prefilled with the oil phase. In case the fluidic capacitor is coupled with the main device, this is connected to the outlet of the transversal microchannel (outlet C, see **Figure 1b**), by a PTFE capillary (OD/ID=0.6 mm/0.3 mm, Sigma Aldrich). A flowmeter (M size, by Fluigent) is also placed in between the device and fluidic capacitor to monitor the flow-rate ϕ in this portion of the fluidic circuit. The outlet of the fluidic capacitor is connected to a pinch valve. Importantly, prior to droplet flowing, the whole microfluidic circuit is prefilled with oil and the valve is then closed, maintaining this state during the entire experimental workflow, thus assuring a zero-average flow ϕ in the transversal channel. Consequently, since the latter is a dead-end channel, the variations of ϕ are due to the eventual expansion or compression of the fluidic capacitor. In both configurations (with and without the fluidic capacitor), the magnetic microstructures integrated in the device are magnetized by a permanent magnet (NdFeB, N52, 20 mm x 20 mm x 30 mm, by ChenYang Technologies), mounted on a linear translation stage (DDSM50, Thorlabs) with its magnetization direction parallel to the main channel (see **Figure 1a,b**). Therefore, by reducing

the distance between the magnet and the device (D), the structures are magnetized, thus they can be switched ON (D≃3 mm) and OFF (D≃18 mm). Finally, a CMOS camera (acA800-510um, by Basler), installed on a stereo-microscope (by Olympus), is used for the droplet dynamics observation in the device. Data analysis is performed by ImageJ software and LabVIEW (National Instrument) home-made scripts, following the workflow described in[9].

Dispersed phase solutions: According to the performed experiment, different aqueous fluids are used as droplet phase. Milli-Q water and suspension of 1µm size COOH-coated (Dynabeads MyOne Carboxylic Acid) are used during the device optimization, while oligodT-coated paramagnetic particles (1 µm, Dynabeads Oligo(dT)25, by ThermoFisher Scientific) and serial dilutions of a total-RNA sample are used for the mRNA purification and RT-qPCR experiments. During these experiments, three negative controls are also considered by using a water droplet instead of the total RNA sample. Notably, the two types of magnetic particles used in this work, present the same magnetic properties.

The total RNA samples are extracted from SKBR3 human cell line (by ATCC® HTB-30™) by silica-membrane spin columns (RNeasy Mini Kit by Qiagen) and quantified by QuBit (by ThermoFisher Scientific). Then, desired total RNA quantities are diluted into the Binding Buffer provided with the Dynabeads Oligo(dT)25 Kit.

CellsDirect™ One-Step Kit (by ThermoFisher Scientific) is used to prepare the RT-qPCR mix as follows: 12.5 µL of 2X Reaction Mix, 1 µL of each Forward and Reverse primers (10 µM, custom primers to study HER2 or ACTB from Integrated DNA Technologies), 0.5 µL of FAM hydrolysis probe (10 µM, from Integrated DNA Technologies), 1 µL of SuperScript® III RT/Platinum® Taq Mix and DEPC-treated water in a quantity sufficient for reaching 25 µL. Smart Cycler (by Cepheid) is used for RT-qPCR analysis.

Numerical simulation settings: The numerical model considers three different magnetic elements spatially arranged as in the experimental conditions: i) the external permanent magnet; ii) the soft magnetic microstructures and iii) the paramagnetic particles transported by the

droplet. In the magnetic dipole approximation, the magnetic force $\mathbf{F_{mag}}$ acting on a cluster of particles can be approximated as: $\mathbf{F_{mag}} \simeq Q/\rho \cdot M(\mathbf{B_p}) \cdot \nabla \mathbf{B_p}$, where **Q**, ρ and **M** are the particles quantity, density and magnetization respectively, while $\mathbf{B_p}$ is the local magnetic flux density experienced by the particles[6]. Differently, the integrated soft magnetic structures, fabricated in various magnetic PDMS formulations, are defined by the equation $\mathbf{B_p}=\mu_0\mu_r\mathbf{H}$, where μ_0 and μ_r are the vacuum and the material permeability, respectively[33],[34]. The magnetization of the permanent magnet is fixed at 10^6 A/m, according with the supplier specifications, and **H** is the related magnetic field generated in the space (defined as air).

Supporting Information
Supporting Information is available from the Wiley Online Library or from the author.

Acknowledgements
The authors acknowledge Giorgio Delfitto for fruitful discussions about the equivalent electric/fluidic circuit. This work was supported by the French National Research Agency (ANR) as part of the "Investissements d'Avenir" program (reference: ANR10-NANO0207 and Labex and Equipex IPGG), ARC foundation for young researcher fellowship (D. F.) and ERC Advanced Grant CellO (FP7-IDEAS-ERC-321107). MS was supported by a Curie Institute International PhD fellowship.

Received: ((will be filled in by the editorial staff))
Revised: ((will be filled in by the editorial staff))
Published online: ((will be filled in by the editorial staff))

References

[1] L. Shang, Y. Cheng, Y. Zhao, *Chem. Rev.* **2017**, *117*, 7964.

[2] D. Pekin, Y. Skhiri, J.-C. Baret, D. Le Corre, L. Mazutis, C. Ben Salem, F. Millot, A. El Harrak, J. B. Hutchison, J. W. Larson, D. R. Link, P. Laurent-Puig, A. D. Griffiths, V. Taly, *Lab Chip* **2011**, *11*, 2156.

[3] J. Shim, R. T. Ranasinghe, C. A. Smith, S. M. Ibrahim, F. Hollfelder, W. T. S. Huck, D. Klenerman, C. Abell, *ACS Nano* **2013**, *7*, 5955.

[4] E. Z. Macosko, A. Basu, R. Satija, J. Nemesh, K. Shekhar, M. Goldman, I. Tirosh, A. R. Bialas, N. Kamitaki, E. M. Martersteck, J. J. Trombetta, D. A. Weitz, J. R. Sanes, A. K. Shalek, A. Regev, S. A. McCarroll, *Cell* **2015**, *161*, 1202.

[5] A. M. Klein, L. Mazutis, I. Akartuna, N. Tallapragada, A. Veres, V. Li, L. Peshkin, D. A. Weitz, M. W. Kirschner, *Cell* **2015**, *161*, 1187.

[6] M. Serra, D. Ferraro, I. Pereiro, J.-L. Viovy, S. Descroix, *Lab Chip* **2017**, DOI 10.1039/C7LC00582B.

[7] D. Lombardi, P. S. Dittrich, *Anal. Bioanal. Chem.* **2011**, *399*, 347.

[8] E. Al-Hetlani, O. J. Hatt, M. Vojtíšek, M. D. Tarn, A. Iles, N. Pamme, in *8th Int. Conf. Sci. Clin. Appl. Magn. Carriers. AIP Conf. Proc.*, **2010**, pp. 167–175.

[9] M. Serra, T. D. Mai, A. L. Serra, M.-C. Nguyen, A. Eisele, L. Perié, J.-L. Viovy, D. Ferraro, S. Descroix, *Sensors Actuators B Chem.* **2019**, 127346.

[10] R. Gao, Z. Cheng, A. J. DeMello, J. Choo, *Lab Chip* **2016**, *16*, 1022.

[11] H. Lee, L. Xu, K. W. Oh, *Biomicrofluidics* **2014**, *8*, 044113.

[12] E. Brouzes, T. Kruse, R. Kimmerling, H. H. Strey, *Lab Chip* **2015**, *15*, 908.

[13] B. Verbruggen, T. Tóth, M. Cornaglia, R. Puers, M. A. M. Gijs, J. Lammertyn, *Microfluid. Nanofluidics* **2015**, *18*, 91.

[14] B. Verbruggen, K. Leirs, R. Puers, J. Lammertyn, *Microfluid. Nanofluidics* **2015**, *18*, 293.

[15] X. Niu, S. Gulati, J. B. Edel, A. J. deMello, *Lab Chip* **2008**, *8*, 1837.

[16] M. Chabert, K. D. Dorfman, J.-L. Viovy, *Electrophoresis* **2005**, *26*, 3706.

[17] D. Ferraro, J. Champ, B. Teste, M. Serra, L. Malaquin, J.-L. Viovy, P. De Cremoux, S. Descroix, *Sci. Rep.* **2016**, *6*, DOI 10.1038/srep25540.

[18] Y. J. Kang, S. Yang, *Lab Chip* **2012**, *12*, 1881.

[19] D. C. Leslie, C. J. Easley, E. Seker, J. M. Karlinsey, M. Utz, M. R. Begley, J. P. Landers, *Nat. Phys.* **2009**, *5*, 231.

[20] P. N. Duncan, T. V. Nguyen, E. E. Hui, *Proc. Natl. Acad. Sci. U. S. A.* **2013**, *110*, 18104.

[21] R. R. Collino, N. Reilly-Shapiro, B. Foresman, K. Xu, M. Utz, J. P. Landers, M. R. Begley, *Lab Chip* **2013**, *13*, 3668.

[22] Cancer Genome Atlas Network, *Nature* **2012**, *490*, 61.

[23] M. Faivre, R. Gelszinnis, J. Degouttes, N. Terrier, C. Rivière, R. Ferrigno, A.-L. Deman, *Biomicrofluidics* **2014**, *8*, 054103.

[24] R. Zhou, C. Wang, *Microfluid. Nanofluidics* **2016**, *20*, 48.

[25] B. Teste, N. Jamond, D. Ferraro, J.-L. Viovy, L. Malaquin, *Microfluid. Nanofluidics* **2015**, *19*, 141.

[26] M. Ochsner, M. R. Dusseiller, H. M. Grandin, S. Luna-Morris, M. Textor, V. Vogel, M. L. Smith, *Lab Chip* **2007**, *7*, 1074.

[27] Y. Fouillet, C. Parent, G. Gropplero, L. Davoust, J. L. Achard, F. Revol-Cavalier, N.

Verplanck, Y. Fouillet, C. Parent, G. Gropplero, L. Davoust, J. L. Achard, F. Revol-Cavalier, N. Verplanck, *Proceedings* **2017**, *1*, 501.

[28] S. Park, K. Mondal, R. M. Treadway, V. Kumar, S. Ma, J. D. Holbery, M. D. Dickey, *ACS Appl. Mater. Interfaces* **2018**, *10*, 11261.

[29] L. Ménétrier-Deremble, P. Tabeling, *Phys. Rev. E* **2006**, *74*, 035303.

[30] J. Bergstrom, *Mechanics of Solid Polymers : Theory and Computational Modeling*, **n.d.**

[31] K. W. Oh, K. Lee, B. Ahn, E. P. Furlani, *Lab Chip* **2012**, *12*, 515.

[32] H. J. M. de Jonge, R. S. N. Fehrmann, E. S. J. M. de Bont, R. M. W. Hofstra, F. Gerbens, W. A. Kamps, E. G. E. de Vries, A. G. J. van der Zee, G. J. te Meerman, A. ter Elst, *PLoS One* **2007**, *2*, e898.

[33] J. Li, M. Zhang, L. Wang, W. Li, P. Sheng, W. Wen, *Microfluid. Nanofluidics* **2011**, *10*, 919.

*[34] J. Keyes, M. Junkin, P. K. Wong, J. P. Vande Geest, Biomed. Microdevices **2009**, 11, 1259-67.*